

A topology optimization of open acoustic waveguides based on a scattering matrix method

Kei Matsushima^{a,*}, Hiroshi Isakari^b, Toru Takahashi^c, Toshiro Matsumoto^c

^a*The University of Tokyo, 2-11-16 Yayoi, Bunkyo-ku, Tokyo, Japan*

^b*Keio University, 3-14-1 Hiyoshi, Kohoku-ku, Yokohama, Kanagawa, Japan*

^c*Nagoya University, Furo-cho, Chikusa-ku, Nagoya, Aichi, Japan*

Abstract

This study presents a topology optimization scheme for realizing a bound state in the continuum along an open acoustic waveguide comprising a periodic array of elastic materials. First, we formulate the periodic problem as a system of linear algebraic equations using a scattering matrix associated with a single unit structure of the waveguide. The scattering matrix is numerically constructed using the boundary element method. Subsequently, we employ the Sakurai–Sugiura method to determine resonant frequencies and the Floquet wavenumbers by solving a nonlinear eigenvalue problem for the linear system. We design the shape and topology of the unit elastic material such that the periodic structure has a real resonant wavenumber at a given frequency by minimizing the imaginary part of the resonant wavenumber. The proposed topology optimization scheme is based on a level-set method with a novel topological derivative. We demonstrate a numerical example of the proposed topology optimization and show that it realizes a bound state in the continuum through some numerical experiments.

Keywords: Bound state in the continuum, Topology optimization, Acoustic waveguide, Scattering matrix, Boundary element method

2010 MSC: 00-01, 99-00

*Corresponding author

1. Introduction

Recently, bound states in the continuum (BICs) have been enthusiastically investigated in the fields of quantum mechanics, photonics, acoustics, and water waves [1]. BICs were originally proposed by von Neumann and Wigner [2] in a quantum system and then experimentally found in some classical systems [3–5]. Historically, it has been said that bound states can exist only outside the radiation continuum, where a near-field state cannot be coupled to any radiation (scattering) channel, resulting in a perfectly confined state in the vicinity of a structure. Challenging this conventional wisdom, BICs may exist within the continuum in some geometrical systems, e.g., waveguides [6, 7] and photonic/phononic crystal slabs (diffraction gratings) [4, 5, 8, 9]. BICs are of theoretical interest and practical importance due to their potential to realize high-Q resonance, which is an essential property of lasers [10], filters [11], and sensors [12] for next generations.

Because resonance properties are sensitive to the material and geometrical configurations of a structure, some inverse-design approaches, such as parameter tuning and shape/topology optimization [13, 14], may be necessary to realize high-Q resonance originating from BICs in practical applications [1]. Such optimization techniques have been recently used to design some photonic and phononic structures with maximized bandgaps [15]. Though BICs are formulated similar to photonic/phononic bandgaps, we encounter some numerical difficulties when applying optimization-based design methods to manipulate BICs because they often rely on finite element methods.

BICs are formulated as resonant states satisfying Maxwell’s or Helmholtz’ equations in open systems and characterized as an eigenmode of a nonlinear eigenvalue problem to find a frequency and wavenumber that allow a nonzero state without any incident field. For some simple geometries, we can employ a semianalytical technique, such as cylindrical or spherical wave expansions [9], to effectively compute resonant states. For example, Evans and Porter showed numerical evidence that a circular inclusion in a planar waveguide supports BICs

[16]. Later, rectangular scatterers are considered by Porter and Evans [17]. The recent work by Bennetts and Peter investigated arrays of circular scatterers in water based on a transfer operator with cylindrical functions [18]. See the review by Linton and McIver for more details [6]. However, more general configurations require a discretization-based method, such as the finite element method and boundary element method (BEM). These methods should be carefully implemented to avoid neglecting the radiation effect of BICs because resonant states in open systems are not bounded or even diverging in space [19]. This is not the case for the photonic bandgap computation because the underlying eigenvalue problem is defined in a bounded domain.

After the numerical analysis of BICs, we need to calculate the sensitivity of their eigenvalues for structural optimization, which is called design sensitivity. Because the corresponding boundary value problem is defined in an open space, we need to truncate the unbounded domain and to carefully deal with the truncated boundary through some special treatment, such as the Dirichlet-to-Neumann map to evaluate the variation in the eigenvalue with respect to geometrical perturbation [20]. This would incur additional computational cost (especially when the BEM is used) because the variation involves a volume integral of the resonant state over the truncated domain. To the authors' best knowledge, no prior works have found design sensitivity for BICs.

Therefore, this study proposes a topology optimization scheme for designing open acoustic waveguides exhibiting BICs at desired frequencies in two dimensions to overcome the above difficulties. First, we propose a scattering matrix-based approach to compute BICs. The basic idea is the same as the one proposed in [9], which calculates BICs along a periodic array of circular rods. For the topology optimization, we incorporate the BEM into the scattering matrix method to deal with more geometrically complex structures than the circular rods [21]. Further, we formulate the topological derivative [22] of a resonant wavenumber based on the scattering matrix method. This formulation does not require any volume integration of resonant states; thus, it saves considerable computational costs. Subsequently, we incorporate the topological

derivative into a level set-based topology optimization algorithm [23]. Finally, we perform the topology optimization and numerically demonstrate that the optimized structure forms a BIC.

2. Scattering by multiple and periodic obstacles

In this section, we first formulate wave scattering by multiple and periodic obstacles in two dimensions using the scattering matrix method. Further, we describe how to compute the eigenvalues of the systems.

2.1. Scattering through a single obstacle

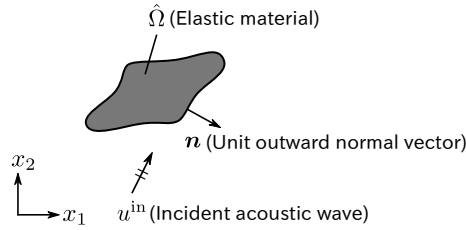


Figure 1: Scattering through a single scatterer $\hat{\Omega}$ placed in the two-dimensional space \mathbb{R}^2 .

As shown in Figure 1, we first consider a scattering problem where a single elastic material $\hat{\Omega}$ is placed in the free space \mathbb{R}^2 . Throughout this paper, we neglect the shear modulus and formulate the time-harmonic scattering problem using the following transmission problem:

$$\nabla^2 u(\mathbf{x}) + \frac{\omega^2}{c^2} u(\mathbf{x}) = 0 \quad x \in \Omega := \mathbb{R}^2 \setminus \overline{\hat{\Omega}}, \quad (1)$$

$$\nabla^2 u(\mathbf{x}) + \frac{\omega^2}{\hat{c}^2} u(\mathbf{x}) = 0 \quad x \in \hat{\Omega}, \quad (2)$$

$$u(\mathbf{x}) := u|_+(\mathbf{x}) = u|_-(\mathbf{x}) \quad x \in \partial\hat{\Omega}, \quad (3)$$

$$q(\mathbf{x}) := \frac{1}{\rho} \frac{\partial u}{\partial n} \Big|_+(\mathbf{x}) = \frac{1}{\hat{\rho}} \frac{\partial u}{\partial n} \Big|_-(\mathbf{x}) \quad x \in \partial\hat{\Omega}, \quad (4)$$

$$\left| \frac{\partial}{\partial r} (u - u^{\text{in}}) - ik(u - u^{\text{in}}) \right| = O(r^{-1/2}) \quad \text{as } r = |\mathbf{x}| \rightarrow \infty, \quad (5)$$

where u denotes the sound pressure, $k = \omega/c$ the wavenumber, and u^{in} the corresponding incident wave. The overline denotes the closure of a domain. A vector quantity \mathbf{p} associated with the Cartesian coordinate system (x_1, x_2) is denoted by a bold symbol, and its components are expressed by p_i ($i = 1, 2$). In addition, $\frac{\partial}{\partial n} = \mathbf{n} \cdot \nabla$ denotes the normal derivative with the unit outward normal vector \mathbf{n} to $\hat{\Omega}$. (5) represents the Sommerfeld radiation condition. Throughout the paper, the time dependence of the time-harmonic fields is chosen as $e^{-i\omega t}$ with the angular frequency ω . In the exterior medium Ω and scatterer $\hat{\Omega}$, the phase velocities c and \hat{c} are given by their mass densities ρ and $\hat{\rho}$ and bulk moduli κ and $\hat{\kappa}$ as $c = \sqrt{\kappa/\rho}$ and $\hat{c} = \sqrt{\hat{\kappa}/\hat{\rho}}$, respectively. The symbol $|_+$ (resp. $|_-$) denotes the trace from Ω (resp. $\hat{\Omega}$) to the boundary.

2.2. Scattering matrix

2.2.1. Definition

Using Graf's addition theorem, which is given by

$$\begin{aligned} & H_n^{(1)}(k|\mathbf{x} - \mathbf{y}|)e^{in\theta(\mathbf{x}-\mathbf{y})} \\ &= \begin{cases} \sum_{m=-\infty}^{\infty} H_m^{(1)}(k|\mathbf{x}|)J_{m-n}(k|\mathbf{y}|)e^{im\theta(\mathbf{x})}e^{-i(m-n)\theta(\mathbf{y})} & (|\mathbf{x}| > |\mathbf{y}|) \\ \sum_{m=-\infty}^{\infty} J_m(k|\mathbf{x}|)H_{m-n}^{(1)}(k|\mathbf{y}|)e^{im\theta(\mathbf{x})}e^{-i(m-n)\theta(\mathbf{y})} & (|\mathbf{x}| < |\mathbf{y}|) \end{cases} \quad (6) \end{aligned}$$

for the Hankel function $H_n^{(1)}$ of the first kind and Bessel function J_n of order n with $\theta(\mathbf{x}) = \tan^{-1}(x_2/x_1)$, we have the multipole expansion of the fundamental solution $G(\mathbf{x}, \mathbf{y}) = \frac{i}{4}H_0^{(1)}(k|\mathbf{x} - \mathbf{y}|)$ as

$$G(\mathbf{x}, \mathbf{y}) = \frac{i}{4} \sum_{n=-\infty}^{\infty} H_n^{(1)}(k|\mathbf{x} - \mathbf{x}_0|)J_n(k|\mathbf{y} - \mathbf{x}_0|)e^{in\theta(\mathbf{x}-\mathbf{x}_0)}e^{-in\theta(\mathbf{y}-\mathbf{x}_0)} \quad (7)$$

for any $\mathbf{x}_0 \in \mathbb{R}^2$ and (\mathbf{x}, \mathbf{y}) satisfying $|\mathbf{x} - \mathbf{x}_0| > |\mathbf{y} - \mathbf{x}_0|$. Substituting this series into the following representation formula

$$u(\mathbf{x}) = u^{\text{in}}(\mathbf{x}) - \rho \int_{\partial\hat{\Omega}} G(\mathbf{x}, \mathbf{y})q(\mathbf{y})d\Gamma_{\mathbf{y}} + \int_{\partial\hat{\Omega}} \frac{\partial G}{\partial n_{\mathbf{y}}}(\mathbf{x}, \mathbf{y})u(\mathbf{y})d\Gamma_{\mathbf{y}} \quad \mathbf{x} \in \Omega, \quad (8)$$

we obtain that the solution u can also be written in terms of the cylindrical functions as follows:

$$u(\mathbf{x}) = u^{\text{in}}(\mathbf{x}) + \sum_{n=-\infty}^{\infty} B_n O_n(\mathbf{x} - \mathbf{x}_0) \quad \mathbf{x} \in \Omega \setminus \overline{D}, \quad (9)$$

$$B_n = \frac{i(-1)^n}{4} \langle I_{-n}, u \rangle_{\partial\hat{\Omega}}, \quad (10)$$

$$I_n(\mathbf{x}) = J_n(k|\mathbf{x}|) e^{in\theta(\mathbf{x})}, \quad (11)$$

$$O_n(\mathbf{x}) = H_n^{(1)}(k|\mathbf{x}|) e^{in\theta(\mathbf{x})}, \quad (12)$$

where $\langle \cdot, \cdot \rangle$ denotes the bilinear form defined by the following boundary integral:

$$\langle v, u \rangle_{\partial\hat{\Omega}} = \int_{\partial\hat{\Omega}} \left(\frac{\partial v}{\partial n} \Big|_+ u|_+ - v|_+ \frac{\partial u}{\partial n} \Big|_+ \right) d\Gamma, \quad (13)$$

and $D = \{\mathbf{x} \in \mathbb{R}^2 \mid |\mathbf{x} - \mathbf{x}_0| < \max_{\mathbf{y} \in \partial\hat{\Omega}} |\mathbf{y} - \mathbf{x}_0|\}$ denotes the minimum enclosing disk of $\hat{\Omega}$ centered at \mathbf{x}_0 . The representation (9) implies that the coefficient vector $B = (B_n)_{n \in \mathbb{Z}}$ completely describes the field u in the exterior of the disk D .

We suppose that the incident wave u^{in} can also be expanded into the cylindrical functions as follows:

$$u^{\text{in}}(\mathbf{x}) = \sum_{n=-\infty}^{\infty} A_n I_n(\mathbf{x} - \mathbf{x}_0) \quad \mathbf{x} \in \Omega \setminus \overline{D} \quad (14)$$

with complex coefficients $A_n \in \mathbb{C}$. For example, when u^{in} is the plane wave $e^{ik\mathbf{p} \cdot (\mathbf{x} - \mathbf{x}_0)}$ propagating along a unit vector $\mathbf{p} \in \mathbb{R}^2$, we have $A_n = (p_2 + ip_1)^n$. From the linearity of the scattering problem (1)–(5), the relationship between the incident coefficient vector $A = (A_n)_{n \in \mathbb{Z}}$ and B should also be linear, which yields the linear equation

$$B_n = \sum_{n'=-\infty}^{\infty} S_{nn'} A_{n'}. \quad (15)$$

The matrix S is called a *scattering matrix*. In what follows, such equation is simply denoted using the matrix-vector notation $B = SA$. For a given vector A , we can compute the multiplication $B = SA$ as follows:

1. Set the incident wave $u^{\text{in}}(\mathbf{x}) = \sum_{n=-\infty}^{\infty} A_n I_n(\mathbf{x} - \mathbf{x}_0)$.

2. Solve the scattering problem (1)–(5) for a given shape $\hat{\Omega}$ and compute u and q on $\partial\hat{\Omega}$.
3. Compute the boundary integral (10).

See [21] for details.

2.2.2. Boundary element method

Once we have a scattering matrix for the scattering problem (1)–(5), the scattered field is uniquely determined using (9) and (15). From the definition (15), each component of the scattering matrix S is given by $S_{nn'} = \langle I_{-n}, u_{n'} \rangle_{\partial\hat{\Omega}}$, where $u_{n'}$ denotes the solution of the boundary value problem (1)–(5) for $u^{\text{in}} = I_{n'}$. Such a solution can be obtained by solving an appropriate boundary integral equation. In this study, we use the Burton–Miller-type boundary integral equation [24], which is given by

$$\begin{bmatrix} \frac{1}{2}\mathcal{I} - \mathcal{D} - \eta\mathcal{N} & \rho(\mathcal{S} + \eta(\frac{1}{2}\mathcal{I} + \mathcal{D}^*)) \\ \frac{1}{2}\mathcal{I} + \hat{\mathcal{D}} & -\hat{\rho}\hat{\mathcal{S}} \end{bmatrix} \begin{pmatrix} u_{n'} \\ q_{n'} \end{pmatrix} = \begin{pmatrix} I_{n'} + \eta\frac{\partial I_{n'}}{\partial n} \\ 0 \end{pmatrix}, \quad (16)$$

for $u_{n'}$ and $q_{n'} = \frac{1}{\rho}\frac{\partial u_{n'}}{\partial n}|_+$ with coupling parameter $\eta \in \mathbb{C}$, where the integral operators \mathcal{S} , \mathcal{D} , \mathcal{D}^* , and \mathcal{N} are respectively defined as

$$(\mathcal{S}\phi)(\mathbf{x}) = \int_{\partial\hat{\Omega}} G(\mathbf{x}, \mathbf{y})\phi(\mathbf{y})d\Gamma_{\mathbf{y}}, \quad (17)$$

$$(\mathcal{D}\phi)(\mathbf{x}) = \int_{\partial\hat{\Omega}} \frac{\partial G}{\partial n_{\mathbf{y}}}(\mathbf{x}, \mathbf{y})\phi(\mathbf{y})d\Gamma_{\mathbf{y}}, \quad (18)$$

$$(\mathcal{D}^*\phi)(\mathbf{x}) = \int_{\partial\hat{\Omega}} \frac{\partial G}{\partial n_{\mathbf{x}}}(\mathbf{x}, \mathbf{y})\phi(\mathbf{y})d\Gamma_{\mathbf{y}}, \quad (19)$$

$$(\mathcal{N}\phi)(\mathbf{x}) = \text{p.f.} \int_{\partial\hat{\Omega}} \frac{\partial^2 G}{\partial n_{\mathbf{x}}\partial n_{\mathbf{y}}}(\mathbf{x}, \mathbf{y})\phi(\mathbf{y})d\Gamma_{\mathbf{y}}, \quad (20)$$

and “p.f.” represents the finite part of the divergent integral. Moreover, the other operators $\hat{\mathcal{S}}$ and $\hat{\mathcal{D}}$ are obtained by replacing c in \mathcal{S} and \mathcal{D} with \hat{c} , respectively. The parameter $\eta \in \mathbb{C}$ is introduced to avoid fictitious eigenvalues, at which the the boundary integral equation becomes ill-posed [24]. Although η is arbitrary as long as $\text{Im}[\eta] < 0$, the formula $\eta = -i/k$ is known to be the best choice in terms of the condition number of a discretized system [25].

2.3. Scattering through a finite number of obstacles

Next, we describe a scattering-matrix formalism to solve multiple scattering problems. See [26, 27] for details.

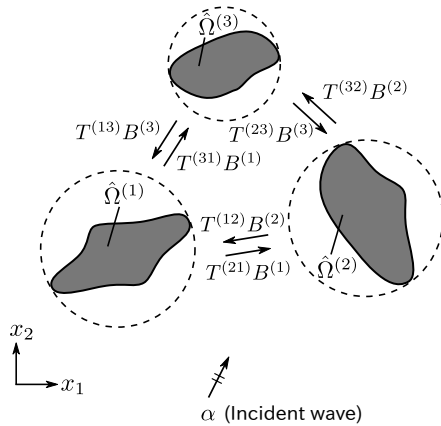


Figure 2: Scattering through multiple scatterers $\hat{\Omega}^{(i)}$ placed in the two-dimensional space \mathbb{R}^2

As shown in Figure 2, we consider the scattering through N scatterers $\hat{\Omega}^{(i)}$ ($i = 1, \dots, N$). The shapes and materials of the scatterers are not necessarily identical. Let $S^{(i)}$ denote the scattering matrix associated with the scatterer $\hat{\Omega}^{(i)}$. The only assumption here is that any minimum disk $D^{(i)}$ enclosing $\hat{\Omega}^{(i)}$, whose center is denoted by $\mathbf{x}_0^{(i)}$, does not overlap with each other (well-separated condition).

Under this assumption, we can write the total field as follows:

$$u(\mathbf{x}) = u^{\text{in}}(\mathbf{x}) + \sum_{i=1}^N \sum_{n=-\infty}^{\infty} B_n^{(i)} O_n(\mathbf{x} - \mathbf{x}_0^{(i)}) \quad \mathbf{x} \in \mathbb{R}^2 \setminus \overline{\cup_{i=1}^N D^{(i)}} \quad (21)$$

for outgoing multipole coefficients $B^{(i)} = (B_n^{(i)})_{n \in \mathbb{Z}}$ associated with $\hat{\Omega}^{(i)}$. Our task is to describe relations among $B^{(1)}, \dots, B^{(N)}$ using the scattering matrices $S^{(i)}$. If \mathbf{x} is located around $D^{(j)}$, i.e., $\mathbf{x} \in \mathbb{R}^2 \setminus \overline{\cup_{i=1}^N D^{(i)}}$ and $\forall i, |\mathbf{x} - \mathbf{x}_0^{(j)}| <$

$|\mathbf{x}_0^{(i)} - \mathbf{x}_0^{(j)}|$ hold, then we can use the formula (6) to obtain

$$\begin{aligned}
& \sum_{n=-\infty}^{\infty} B_n^{(i)} O_n(\mathbf{x} - \mathbf{x}_0^{(i)}) \\
&= \sum_{n=-\infty}^{\infty} B_n^{(i)} H_n^{(1)}(k|\mathbf{x} - \mathbf{x}_0^{(j)} - (\mathbf{x}_0^{(i)} - \mathbf{x}_0^{(j)})|) e^{in\theta(\mathbf{x} - \mathbf{x}_0^{(j)} - (\mathbf{x}_0^{(i)} - \mathbf{x}_0^{(j)}))} \\
&= \sum_{n=-\infty}^{\infty} \left(\sum_{m=-\infty}^{\infty} H_{m-n}^{(1)}(k|\mathbf{x}_0^{(j)} - \mathbf{x}_0^{(i)}|) e^{i(m-n)\theta(\mathbf{x}_0^{(j)} - \mathbf{x}_0^{(i)})} B_n^{(i)} \right) J_n(k|\mathbf{x} - \mathbf{x}_0^{(j)}|) e^{in\theta(\mathbf{x} - \mathbf{x}_0^{(j)})} \\
&= \sum_{n=-\infty}^{\infty} \left(T^{(ji)} B^{(i)} \right)_n I_n(\mathbf{x} - \mathbf{x}_0^{(j)}), \tag{22}
\end{aligned}$$

where $T_{nm}^{(ji)} = O_{m-n}(\mathbf{x}_0^{(j)} - \mathbf{x}_0^{(i)})$ denotes a translation matrix from i th to j th scatterer. The translation formula (22) indicates that the outgoing wave $B^{(i)}$ from $\hat{\Omega}^{(i)}$ turns into the incoming wave $T^{(ji)} B^{(i)}$ around $\hat{\Omega}^{(j)}$. We also assume that the incident wave u^{in} allows the cylindrical expansion written as

$$u^{\text{in}}(\mathbf{x}) = \sum_{n=-\infty}^{\infty} \alpha_n^{(i)} I_n(\mathbf{x} - \mathbf{x}_0^{(i)}) \quad \mathbf{x} \in D^{(i)}, \tag{23}$$

for $i = 1, \dots, N$ and $\alpha^{(i)} = (\alpha_n^{(i)})_{n \in \mathbb{Z}}$. Then, the scattering matrix $S^{(i)}$ relates incoming and outgoing waves around each $\hat{\Omega}^{(i)}$ by

$$S^{(i)} \left(\alpha^{(i)} + \sum_{j \neq i} T^{(ij)} B^{(j)} \right) = B^{(i)}. \tag{24}$$

This linear system solves the unknown vectors $B^{(i)}$ when the incident coefficients $\alpha^{(i)}$ are provided.

The scattering matrices and relevant vectors are of infinite size; thus we have to truncate them in practical computations. We truncate the infinite series $\sum_{n=-\infty}^{\infty}$ into $\sum_{n=-n_{\text{tr}}}^{n_{\text{tr}}}$ using Rokhlin's empirical formula [28] given by

$$n_{\text{tr}} = kd + 8 \log(kd + \pi), \tag{25}$$

where d denotes the minimum distance between two centers, i.e., $d = \min_{i \neq j} |\mathbf{x}_0^{(i)} - \mathbf{x}_0^{(j)}|$.

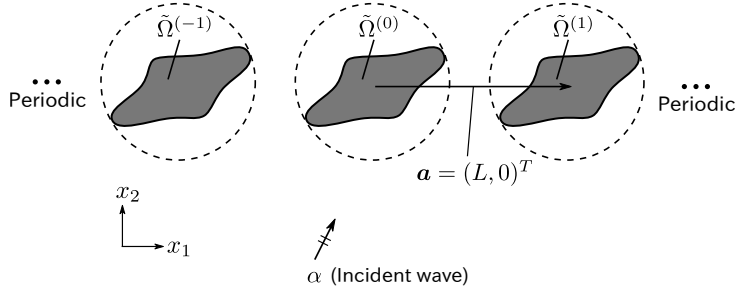


Figure 3: Scattering through a grating comprising periodic scatterers $\hat{\Omega}^{(i)}$ ($i \in \mathbb{Z}$) placed in \mathbb{R}^2

2.4. Scattering through periodic obstacles

2.4.1. Scattering matrix method

Next, we describe a scattering matrix method for wave scattering through periodic obstacles, which was originally proposed in [29] for circular rods. As shown in Figure 3, we consider scatterers periodically embedded along a line in \mathbb{R}^2 . In this study, the lattice vector $\mathbf{a} \in \mathbb{R}^2$ is given by $\mathbf{a} = (L, 0)^T$ without the loss of generality, where $L > 0$ denotes a given constant. We also assume that all scatterers are identical so that $\hat{\Omega}^{(i)}$ ($i \in \mathbb{Z}$) has the same scattering matrix S .

The scattering matrix reduces the periodic scattering problem into a system of linear algebraic equations involving the outgoing multipole coefficients $B^{(i)}$ and incident coefficients $\alpha^{(i)}$ associated with each scatterer $\hat{\Omega}^{(i)}$. To investigate this, we formally use (24) to obtain

$$S \left(\alpha^{(i)} + \sum_{j \neq i, j=-\infty}^{\infty} T^{(ij)} B^{(j)} \right) = B^{(i)}, \quad (26)$$

for each $i \in \mathbb{Z}$. We assume that the incident wave u^{in} has the quasiperiodicity $u^{\text{in}}(\mathbf{x} + \mathbf{a}) = u^{\text{in}}(\mathbf{x})e^{i\beta}$ for a Floquet wavenumber $\beta \in \mathbb{C}$, which is equivalent to $\alpha^{(i+1)} = \alpha^{(i)}e^{i\beta}$. Then, from the Bloch–Floquet theorem, $B^{(i)}$ should satisfy the same quasiperiodic condition $B^{(i+1)} = B^{(i)}e^{i\beta}$. Substituting these conditions

into (26), we obtain

$$(I - S(\omega)T^G(\omega, \beta))B(\omega, \beta) = S(\omega)\alpha(\omega, \beta), \quad (27)$$

where $B = B^{(0)}$ and $\alpha = \alpha^{(0)}$. The matrix T^G is defined by the lattice sum as follows:

$$T_{ij}^G = \sum_{n \in \mathbb{Z} \setminus \{0\}} T_{ij}^{(0n)} e^{in\beta} = \sum_{n \in \mathbb{Z} \setminus \{0\}} O_{j-i}(-n\mathbf{a}) e^{in\beta}. \quad (28)$$

This lattice sum is called a *Schlömilch series* and slowly convergent if $\beta \in \mathbb{R}$ and $\omega > 0$ [30].

Note that the proposed method is closely related to BEM with quasi-periodic Green's function [31–35]. Although these approaches are more straightforward, the scattering matrix formulation is more convenient for evaluating the topological derivative, introduced in Section 3.1.

2.4.2. Integral representation of the Schlömilch series

Although the Schlömilch series (28) is convergent for real ω and β , we need a more rapidly convergent representation to evaluate it numerically. Moreover, we wish to establish a representation that is valid even for complex β and ω to compute resonant frequencies ω and wavenumbers β because they lie in the complex planes.

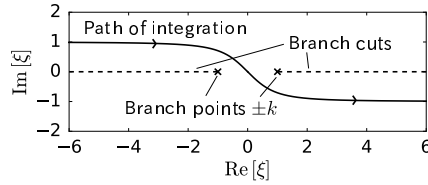


Figure 4: Path of integration for the rightmost term in the RHS of (29) and branch cuts of $R(\xi)$ for $k = 1$

First, we assume that $\omega > 0$ and $\beta \in \mathbb{R}$. According to [32], T^G has the following integral representation:

$$T_{ij}^G = \sum_{n=1}^{s-1} O_{j-i}(-n\mathbf{a})e^{in\beta} + \sum_{n=-s+1}^{-1} O_{j-i}(-n\mathbf{a})e^{in\beta} + \frac{1}{\pi ik^{i-j}} \int_{-\infty}^{\infty} f_{i-j}(\xi)d\xi, \quad (29)$$

$$f_n(\xi) = \frac{e^{s(-i\beta-R(\xi)L)}(\xi - R(\xi))^n}{R(\xi)(1 - e^{-i\beta-R(\xi)L})} + \frac{e^{s(i\beta-R(\xi)L)}(\xi + R(\xi))^n}{R(\xi)(1 - e^{i\beta-R(\xi)L})}, \quad (30)$$

$$R(\xi) = \sqrt{\xi^2 - k^2}, \quad (31)$$

where the integer $s \geq 2$ is arbitrary. This integral representation is a modified version of Linton's integral form [30]. To obtain the convergence of the integral in (29), we have to determine the branch cuts of the integrand, choose an appropriate sheet, and deform the integration path to circumvent the branch cuts. A possible choice is $R(\xi) = \sqrt{|\xi^2 - k^2|} \exp(i\text{Arg}(\xi^2 - k^2)/2)$, where $\text{Arg} : \mathbb{C} \rightarrow (-\pi, \pi]$ is the principal argument. Here, we can choose a path of integration as the steepest descent path of $\exp(-sR(\xi)L)$ to obtain a rapid convergence. Thus, we use the path given by $\xi(t) = \pm Q(t)$ for $t \in [0, \infty)$, where $Q(t) = \sqrt{|t^2 - 2ikt|} \exp(i\text{Arg}(t^2 - 2ikt)/2)$. Figure 4 illustrates the path of integration and branch cuts from which we confirm that the path does not cross the branch cuts. Finally, we obtain

$$\int_{-\infty}^{\infty} f_{i-j}(\xi)d\xi = \int_0^{\infty} \left[f_{i-j}(Q(t)) + f_{i-j}(-Q(t)) \right] \frac{t - ik}{Q(t)} dt. \quad (32)$$

Because the integrand in (32) is oscillatory and has a weak singularity of order $t^{-1/2}$ at $t = 0$, we further apply the double-exponential formula [36] to this integral in the practical computation.

Although the integral expression (29) is originally proposed for real ω and β , the convergence of the Fourier integral (32) is still achieved for complex β

and ω . To see this, let us evaluate the integrand in (32) as follows:

$$\begin{aligned}
& \left[f_n(Q(t)) + f_n(-Q(t)) \right] \frac{t - ik}{Q(t)} \\
&= \frac{1}{\sqrt{t^2 - 2ikt}} \left[\frac{(\sqrt{t^2 - 2ikt} - t + ikt)^n e^{-Lst + is(kL - \beta)}}{1 - e^{-Lt + i(kL - \beta)}} \right. \\
&\quad \left. + \frac{(\sqrt{t^2 - 2ikt} + t - ikt)^n e^{-Lst + is(kL + \beta)}}{1 - e^{-Lt + i(kL + \beta)}} \right] \\
&= O(t^{|n|-1} e^{-sLt}), \quad t \rightarrow +\infty. \tag{33}
\end{aligned}$$

This estimation shows that the integral (32) is convergent even if $\text{Im}[\beta] \neq 0$ or $\text{Im}[\omega] \neq 0$. The representation (32) has an infinite number of branch points at $\beta = 2m\pi \pm kL$ for $m \in \mathbb{Z}$, yielding the Rayleigh anomaly. More careful investigations [34] show that all branch cuts of $\beta \mapsto T^G$ for a fixed ω are written as $\{kL + 2m\pi + iy \mid y \geq 0, m \in \mathbb{Z}\}$ and $\{-kL + 2m\pi - iy \mid y \geq 0, m \in \mathbb{Z}\}$.

In Figure 5, we plot the values of T_{ij}^G calculated using the lattice sum (28) and integral representation (32) with $s = 2$ to validate the expressions. The lattice sum (28) is truncated at $|n| = 10^8$. In this computation, the comparison between (28) and (32) is given only along the real axis because the lattice sum (28) is divergent otherwise. The results show that T_{ij}^G is smoothly extended into the complex β -plane except for the branch cuts. In addition, the values are in good agreement with the truncated lattice sum.

2.5. Modal analysis

The scattering-matrix formalism (27) allows us to perform guided- and leaky-mode analysis by finding pairs (ω, β) such that the linear system (27) has a nontrivial solution B without any incident field α . This is a nonlinear eigenvalue problem for the matrix-valued function $I - ST^G$ when either ω or β is fixed in \mathbb{C} . Therefore, it can be solved using a gradient- or contour integral-based algorithm. In this study, we adopt the Sakurai–Sugiura method (SSM) [37], which determines an eigenpair (z, ϕ) of $F(z)\phi = 0$, where F denotes a matrix-valued and possibly nonlinear function, within a closed path C in \mathbb{C} by integrating $u^H F^{-1} v$ for some u and v on C and converting the nonlinear eigenvalue problem into a generalized eigenvalue problem. The SSM can find multiple

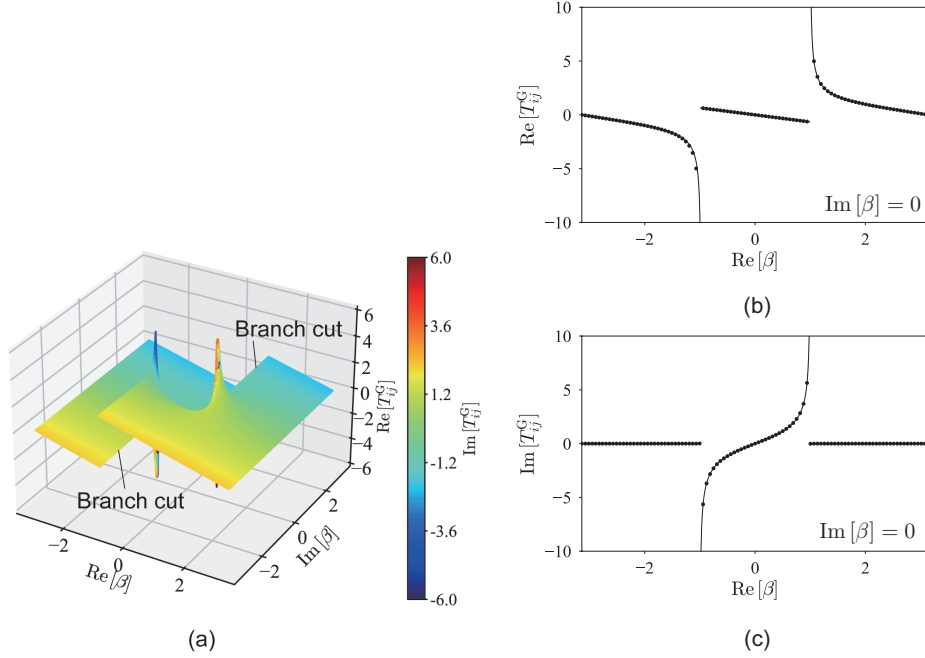


Figure 5: Schlömlich series T_{ij}^G for $i - j = 1$, $k = 1$, and $L = 1$. (a) Values of T_{ij}^G computed using the integral representation (32). (b) and (c) Real and imaginary parts of T_{ij}^G for real β , respectively. The values are calculated using the lattice sum (28) (dots) and integral representation (32) (solid lines).

eigenvalues (even if they are degenerated) in C when an appropriate parameter is given in the algorithm. This approach is originally proposed and validated by Nose and Nishimura [34] with a fast multipole method. They applied the SSM to find nonlinear eigenvalues of a coefficient matrix that arises in a BEM with quasi-periodic Green's function. We refer to [37] for more details about the SSM algorithm.

For a fixed $\omega > 0$, a guided mode propagates along periodic obstacles without attenuation in space, meaning that a resonant wavenumber β is real. On the other hand, if β is complex, the corresponding mode decays exponentially as it travels along the structure. In this case, we say that a resonant mode is leaky. A leaky mode u satisfies the original boundary value problem (1)–(5).

Furthermore, if the pair $\omega > 0$ and $\beta \in \mathbb{R}$ lies in the radiation continuum, i.e., $\omega^2/c^2 - (\beta + 2n\pi)^2/L^2 > 0$ for some $n \in \mathbb{Z}$, then the bound state is called a BIC.

3. Topology optimization

In this section, we design the shape and topology of a unit structure comprising a periodic waveguide such that it exhibits desirable resonant properties. To this end, we use a topology optimization approach [14] to seek an optimal material distribution for a given objective functional. Here, the objective functional is set as $(\text{Im}[\beta])^2$ with a resonant wavenumber β . To apply topology optimization, we need a sensitivity of the given objective functional with respect to a geometrical perturbation, called a topological derivative. In this section, we first derive a novel expression of the topological derivative for the eigenvalue problem in Section 3.1 and then explain the algorithm for the topology optimization in Section 3.2.

3.1. Topological derivative

For an effective optimization algorithm, we need sensitivity with respect to a small perturbation of the geometry of a unit structure. In this subsection, we derive topological derivatives [22] related to resonant properties of the periodic waveguide.

3.1.1. Scattering matrix

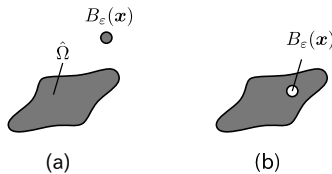


Figure 6: Topological change around a single scatterer $\hat{\Omega}$. (a) Case that a small disk B_ε appears in the exterior Ω . (b) Case that a small disk B_ε appears in the interior $\hat{\Omega}$.

Here, we first investigate the perturbation of the scattering matrix S associated with a single scatterer $\hat{\Omega}$ by a small particle added at a point x in either $\Omega = \mathbb{R}^2 \setminus \overline{\hat{\Omega}}$ or $\hat{\Omega}$. Let $B_\varepsilon(\mathbf{x})$ be an open disk of radius ε centered at x . First, we consider the case of $x \in \Omega$ and assume that the disk $B_\varepsilon(\mathbf{x})$ is characterized by $\hat{\rho}$ and $\hat{\kappa}$, i.e. $B_\varepsilon(\mathbf{x})$ comprises the same material filling in $\hat{\Omega}$, as shown in Figure 6 (a). For sufficiently small radius $\varepsilon > 0$, let δS denote the perturbation of S , i.e.

$$S(\omega; \hat{\Omega} \cup B_\varepsilon(\mathbf{x})) = S(\omega; \hat{\Omega}) + \delta S. \quad (34)$$

Recall that the scattering matrix S is given by

$$S_{nn'} = \frac{i(-1)^n}{4} \langle I_{-n}, u_{n'} \rangle_{\partial \hat{\Omega}}, \quad (35)$$

which yields the variation

$$\delta S_{nn'} = \frac{i(-1)^n}{4} \langle I_{-n}, \delta u_{n'} \rangle_{\partial \hat{\Omega}} + \frac{i(-1)^n}{4} \langle I_{-n}, u_{n'} + \delta u_{n'} \rangle_{\partial B_\varepsilon(\mathbf{x})}, \quad (36)$$

where $u_{n'}$ denotes the solution of the boundary value problem (1)–(5) for $u^{\text{in}}(\mathbf{x}) = I_{n'}(\mathbf{x} - \mathbf{x}_0)$, and $u_{n'} + \delta u_{n'}$ represents the solution of the boundary value problem defined by replacing Ω with $\Omega \setminus \overline{B_\varepsilon(\mathbf{x})}$ in (1)–(5).

Let \tilde{u}_n be an adjoint variable satisfying the Helmholtz equations

$$\nabla^2 \tilde{u}_n(\mathbf{x}) + \frac{\omega^2}{c^2} \tilde{u}_n(\mathbf{x}) = 0 \quad x \in \Omega, \quad (37)$$

$$\nabla^2 \tilde{u}_n(\mathbf{x}) + \frac{\omega^2}{\hat{c}^2} \tilde{u}_n(\mathbf{x}) = 0 \quad x \in \hat{\Omega}, \quad (38)$$

and the Sommerfeld radiation condition. Then, the reciprocity theorem yields

$$\int_{\partial \hat{\Omega} \cup \partial B_\varepsilon(\mathbf{x})} \left(\tilde{u}_n|_+ \frac{\partial \delta u_{n'}}{\partial n} \Big|_+ - \delta u_{n'}|_+ \frac{\partial \tilde{u}_n}{\partial n} \Big|_+ \right) d\Gamma = 0, \quad (39)$$

$$\int_{\partial \hat{\Omega}} \left(\tilde{u}_n|_- \frac{\partial \delta u_{n'}}{\partial n} \Big|_- - \delta u_{n'}|_- \frac{\partial \tilde{u}_n}{\partial n} \Big|_- \right) d\Gamma = 0. \quad (40)$$

From (39) and (40), we have

$$\begin{aligned} & \langle I_{-n}, \delta u_{n'} \rangle_{\partial \hat{\Omega}} \\ &= \langle I_{-n}, \delta u_{n'} \rangle_{\partial \hat{\Omega}} - \frac{1}{\rho} \int_{\partial \hat{\Omega} \cup \partial B_\varepsilon(\mathbf{x})} \left(\tilde{u}_n|_+ \frac{\partial \delta u_{n'}}{\partial n} \Big|_+ - \delta u_{n'}|_+ \frac{\partial \tilde{u}_n}{\partial n} \Big|_+ \right) d\Gamma \\ &= \int_{\partial \hat{\Omega}} \left[\frac{1}{\rho} \frac{\partial \delta u_{n'}}{\partial n} \Big|_+ (-\tilde{u}_n|_+ + \tilde{u}_n|_- - \rho I_{-n}) - \delta u_{n'}|_+ \left(-\frac{1}{\rho} \frac{\partial \tilde{u}_n}{\partial n} \Big|_+ + \frac{1}{\hat{\rho}} \frac{\partial \tilde{u}_n}{\partial n} \Big|_- - \frac{\partial I_{-n}}{\partial n} \right) \right] \\ & \quad + \frac{1}{\rho} \langle \tilde{u}_n, \delta u_{n'} \rangle_{\partial B_\varepsilon(\mathbf{x})}. \end{aligned} \quad (41)$$

Imposing the boundary conditions

$$\tilde{u}_n|_+ = \tilde{u}_n|_- - \rho I_{-n} \quad \mathbf{x} \in \partial\hat{\Omega}, \quad (42)$$

$$\frac{1}{\rho} \frac{\partial \tilde{u}_n}{\partial n} \Big|_+ = \frac{1}{\hat{\rho}} \frac{\partial \tilde{u}_n}{\partial n} \Big|_- - \frac{\partial I_{-n}}{\partial n} \quad \mathbf{x} \in \partial\hat{\Omega}, \quad (43)$$

(41) is reduced to $\langle I_{-n}, \delta u_{n'} \rangle_{\partial\hat{\Omega}} = \frac{1}{\rho} \langle \tilde{u}_n, \delta u_{n'} \rangle_{\partial B_\varepsilon(\mathbf{x})}$. Substituting this into (36), we obtain

$$\begin{aligned} \delta S_{nn'} &= \frac{i(-1)^n}{4} \left(\frac{1}{\rho} \langle \tilde{u}_n, \delta u_{n'} \rangle_{\partial B_\varepsilon(\mathbf{x})} + \langle I_{-n}, u_{n'} + \delta u_{n'} \rangle_{\partial B_\varepsilon(\mathbf{x})} \right), \\ &= \frac{i(-1)^n}{4} \left(\langle I_{-n}, u_{n'} \rangle_{\partial B_\varepsilon(\mathbf{x})} + \langle \frac{1}{\rho} \tilde{u}_n + I_{-n}, \delta u_{n'} \rangle_{\partial B_\varepsilon(\mathbf{x})} \right), \\ &= \frac{i(-1)^n}{4} \langle \frac{1}{\rho} \tilde{u}_n + I_{-n}, \delta u_{n'} \rangle_{\partial B_\varepsilon(\mathbf{x})}. \end{aligned} \quad (44)$$

Here, we have used the reciprocity $\langle I_{-n}, u_{n'} \rangle_{\partial B_\varepsilon(\mathbf{x})} = 0$. From the boundary conditions (42) and (43), we have $\frac{1}{\rho} \tilde{u}_n + I_{-n} = u_{-n}$. This formula further simplifies (44) as follows:

$$\delta S_{nn'} = \frac{i(-1)^n}{4} \langle u_{-n}, \delta u_{n'} \rangle_{\partial B_\varepsilon(\mathbf{x})}. \quad (45)$$

We can no longer simplify the expression (45). However, we are only interested in the asymptotic behavior of δS for $\varepsilon \rightarrow 0$. This can be achieved by expanding $\delta u_{n'}$ with respect to ε around the point x . According to [38], we have

$$\begin{aligned} &\langle u_{-n}, \delta u_{n'} \rangle_{\partial B_\varepsilon(\mathbf{x})} \\ &= \pi \varepsilon^2 \left[\frac{2(\hat{\rho} - \rho)}{\rho + \hat{\rho}} \nabla u_{-n}(\mathbf{x}) \cdot \nabla u_{n'}(\mathbf{x}) + \omega^2 \rho \left(\frac{1}{\hat{\kappa}} - \frac{1}{\kappa} \right) u_{-n}(\mathbf{x}) u_{n'}(\mathbf{x}) \right] + O(\varepsilon^3). \end{aligned} \quad (46)$$

Now, we define a topological derivative of f , denoted by $\mathcal{D}_\Gamma f$, as

$$\mathcal{D}_\Gamma f = \lim_{\varepsilon \rightarrow 0} \frac{\delta f}{\pi \varepsilon^2}, \quad (47)$$

where δf denotes the variation of f due to the topological change. Then, (46) gives the final expression for the topological derivative as follows:

$$\begin{aligned} \mathcal{D}_\Gamma S_{nn'} &= \frac{i(-1)^n}{4} \left[\frac{2(\hat{\rho} - \rho)}{\rho + \hat{\rho}} \nabla u_{-n}(\mathbf{x}) \cdot \nabla u_{n'}(\mathbf{x}) + \omega^2 \rho \left(\frac{1}{\hat{\kappa}} - \frac{1}{\kappa} \right) u_{-n}(\mathbf{x}) u_{n'}(\mathbf{x}) \right] \\ &\quad \mathbf{x} \in \Omega. \end{aligned} \quad (48)$$

We can treat the case of $x \in \hat{\Omega}$ (Figure 6 (b)) in the same manner. In this case, the topological derivative is given by

$$\mathcal{D}_{\text{T}}S_{nn'} = \frac{i(-1)^n}{4} \left[\frac{2(\rho - \hat{\rho})}{\rho + \hat{\rho}} \nabla u_{-n}(\mathbf{x}) \cdot \nabla u_{n'}(\mathbf{x}) + \omega^2 \rho \left(\frac{1}{\kappa} - \frac{1}{\hat{\kappa}} \right) u_{-n}(\mathbf{x}) u_{n'}(\mathbf{x}) \right] \quad \mathbf{x} \in \hat{\Omega}. \quad (49)$$

3.1.2. Resonant wavenumber

The topological perturbation changes the distribution of the resonant frequencies and wavenumbers of the periodic system, characterized by the equation (27) with $\alpha = 0$. We fix ω and investigate the variation in β caused by the topological change.

Suppose that the equation

$$(I - S(\omega; \Omega)T^{\text{G}}(\omega, \beta(\Omega)))B(\omega, \beta(\Omega)) = 0 \quad (50)$$

and its perturbed system

$$(I - S(\omega; \hat{\Omega} \cup B_\varepsilon(\mathbf{x}))T^{\text{G}}(\omega, \beta(\hat{\Omega} \cup B_\varepsilon(\mathbf{x}))))B(\omega, \beta(\hat{\Omega} \cup B_\varepsilon(\mathbf{x}))) = 0 \quad (51)$$

have nontrivial solutions. We evaluate the difference $\delta\beta = \beta(\hat{\Omega} \cup B_\varepsilon(\mathbf{x})) - \beta(\Omega)$.

From (50) and (51), we have

$$S \frac{\partial T^{\text{G}}}{\partial \beta} B \delta\beta = -\delta S T^{\text{G}} B + (I - S T^{\text{G}}) \delta B - \delta S (\delta T^{\text{G}} B + (T^{\text{G}} + \delta T^{\text{G}}) \delta B) - S \delta T^{\text{G}} \delta B. \quad (52)$$

Let \tilde{B} be a left eigenvector satisfying $\tilde{B}^H (I - S T^{\text{G}}) = 0$. Then, multiplying both sides of (52) by \tilde{B}^H , we have

$$\tilde{B}^H S \frac{\partial T^{\text{G}}}{\partial \beta} B \delta\beta = -\tilde{B}^H \delta S T^{\text{G}} B - \tilde{B}^H \delta S (\delta T^{\text{G}} B + (T^{\text{G}} + \delta T^{\text{G}}) \delta B) - \tilde{B}^H S \delta T^{\text{G}} \delta B, \quad (53)$$

which gives the topological derivative

$$\mathcal{D}_{\text{T}}\beta = -\frac{\tilde{B}^H (\mathcal{D}_{\text{T}}S) T^{\text{G}} B}{\tilde{B}^H S \frac{\partial T^{\text{G}}}{\partial \beta} B}. \quad (54)$$

Here, we have neglected the higher-order variations.

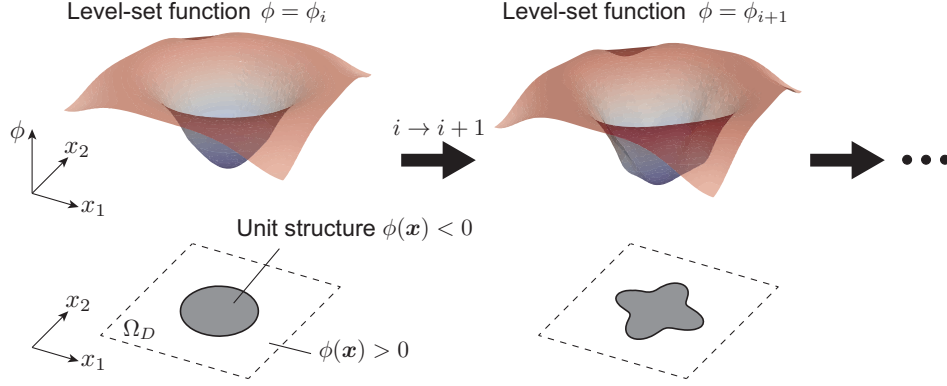


Figure 7: Schematic illustration of the level-set-based topology optimization method.

3.2. Algorithm for the topology optimization

Herein, we perform the topology optimization to find a shape of a unit structure $\hat{\Omega}$ that minimizes the objective functional $J = (\text{Im}[\beta])^2$ for a fixed ω . If the objective value attains $J = 0$, the obtained shape $\hat{\Omega}$ should exhibit a BIC at the target frequency. To this end, we employ a level-set-based topology optimization algorithm.. First, we define a scalar function $\phi : \Omega_D \rightarrow \mathbb{R}$, called a *level-set function*, within a fixed design domain $\Omega_D \subset \mathbb{R}^2$. The level-set function ϕ gives the material distribution in Ω_D by

$$\hat{\Omega} = \{x \in \Omega_D \mid \phi(\mathbf{x}) < 0\}, \quad (55)$$

$$\Omega_D \setminus \overline{\hat{\Omega}} = \{x \in \Omega_D \mid \phi(\mathbf{x}) > 0\}, \quad (56)$$

$$\partial\hat{\Omega} = \{x \in \Omega_D \mid \phi(\mathbf{x}) = 0\}. \quad (57)$$

Instead of seeking an optimal shape of $\hat{\Omega}$ directly, level-set-based topology optimization methods optimize the distribution of ϕ using iterative algorithms. This procedure is illustrated in Figure 7. Following [39], we iteratively update the level-set function ϕ by the following formula:

$$\phi_{i+1}(\mathbf{x}) = (1 - \Delta_i(\mathcal{T}_i, \phi_i)_{L^2(\Omega_D)})\phi_i(\mathbf{x}) + \Delta_i\mathcal{T}_i(\mathbf{x}), \quad (58)$$

where ϕ_i denotes the level-set function at i th step, $\Delta_i > 0$ denotes a step length, \mathcal{T}_i represents the topological derivative of the objective functional J

corresponding to $\hat{\Omega}$ at i th step, and $(\cdot, \cdot)_{L^2(\Omega_D)}$ denotes the L^2 inner product in Ω_D defined by

$$(f, g)_{L^2(\Omega_D)} = \int_{\Omega_D} f(\mathbf{x})g(\mathbf{x})d\Omega, \quad (59)$$

for scalar functions f and g in Ω_D . In the iterative algorithm, the functions ϕ_i and \mathcal{T}_i are discretized using the B-spline basis functions [23]. Once the iterative procedure (58) reaches convergence, we terminate the algorithm and obtain the optimal shape of $\hat{\Omega}$ corresponding to ϕ_i .

4. Numerical examples

In this section, we first verify the proposed method and examine the correctness of the new topological derivative. Subsequently, we present a numerical example of the topology optimization that designs a resonant waveguide exhibiting a BIC at a given frequency.

4.1. Verification of the scattering matrix method

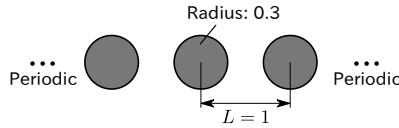


Figure 8: Disks placed periodically in the x_1 direction.

First, we verify that the proposed method determines a BIC accurately. As shown in Figure 8, we consider a waveguide comprising circular elastic materials of radius 0.3 with mass density $\hat{\rho} = 2$ and bulk modulus $\hat{\kappa} = 1$ embedded in the background medium characterized by $\rho = 1$ and $\kappa = 1$. According to [34], this waveguide has a complex eigenvalue $\beta = 0.591931 + 0.034843i$ for $\omega = 6.2831$.

We employ the SSM for a circular contour path C of radius 0.4 centered at $0.5 + 0.0i$ in the complex β -plane to determine the eigenvalue. The SSM algorithm performs contour integration along C using the trapezoidal rule with 32 subintervals. Note that the path C does not cross any branch cut for $\omega =$

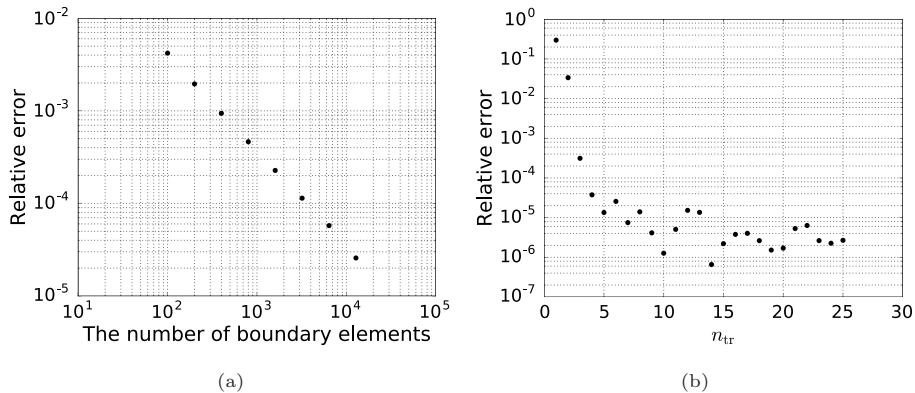


Figure 9: Relative error of an eigenvalue inside the path C . (a) The case when the number of boundary elements varies. (b) The case when the number of terms n_{tr} (defined in Section 2.3) varies.

6.2831. We discretize a unit disk in Figure 8 using piecewise constant boundary elements. The number of boundary elements is denoted by N .

First, we perform the eigenvalue analysis for each $N = N_i$ ($i = 0, 1, \dots, 8$), where N_i is defined as $N_i = 100 \times 2^i$, and fixed $n_{tr} = 20$. Figure 9 (a) shows the relative error of a unique eigenvalue $\beta(N)$ inside C defined by $|\beta(N_{i+1}) - \beta(N_i)|/|\beta(N_i)|$ for each N . The result shows that the relative error decreases monotonically and converges at the rate of $O(N^{-1})$. For $N = 12,800$, the obtained eigenvalue is $\beta = 0.59259 + 0.035012i$, which is close to the value reported in [34]. Further, we fix N at $N = 12,800$ and define a relative error in an analogous manner for $n_{tr} = 1, 2, \dots, 30$. Figure 9 (b) shows the result of the error analysis. The result of the error analysis shows that the error monotonically decreases until it reaches around 10^{-5} , which is close to the value at $N = 12,800$ in Figure 9 (a). From these convergence tests, we conclude that the proposed method can determine resonant wavenumbers correctly.

4.2. Topological derivative

In this section, we examine the correctness of the topological derivative formulated in Section 3.1 through a numerical experiment.

In this experiment, we use the same parameters and configuration as those

used in the previous example. We compare the derivative $(\mathcal{D}_T\beta)(\mathbf{x})$ with the finite difference $(\beta(\hat{\Omega} \cup B_\varepsilon(\mathbf{x})) - \beta(\hat{\Omega})) / (\pi\varepsilon^2)$ for some center x and small radius $\varepsilon > 0$ to verify the topological derivative.

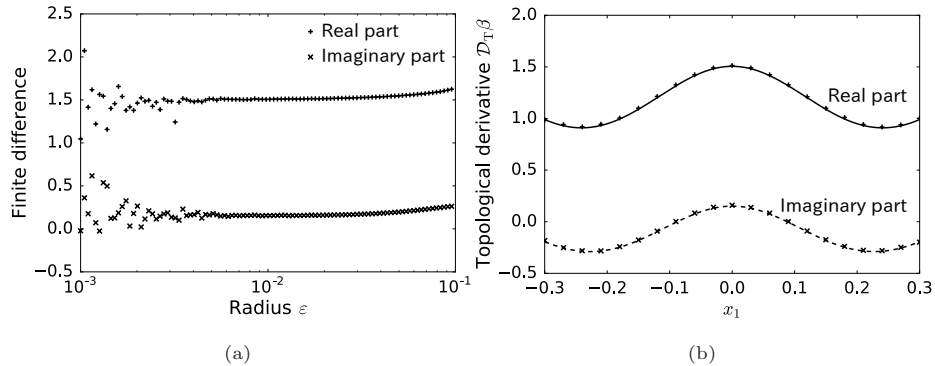


Figure 10: Topological derivatives $(\mathcal{D}_T\beta)(\mathbf{x})$ and finite difference $(\beta(\hat{\Omega} \cup B_\varepsilon(\mathbf{x})) - \beta(\hat{\Omega})) / (\pi\varepsilon^2)$. (a) Finite difference versus the radius ε for $\mathbf{x} = (0.0, 0.4)^T$. (b) Comparison between the topological derivative and finite difference for $\varepsilon = 0.02$ along the line $x_2 = 0.4$. The solid and dashed lines indicate the real and imaginary parts of the topological derivative, respectively. The markers express the finite difference.

First, we fix the center at $\mathbf{x} = (0.0, 0.4)^T$ and investigate an appropriate radius ε . Figure 10 (a) illustrates the behavior of the finite difference approximation of β with respect to the radius ε . The result shows that the approximation almost converges at $\varepsilon = 0.02$ and oscillates for smaller ε due to the loss of significant digits in computing the numerator. Thus, we can expect that $\varepsilon = 0.02$ produces a reasonable approximation to the topological derivative.

Then, we use $\varepsilon = 0.02$ and compare the approximation and topological derivative. Figure 10 (b) shows the approximation and derivative along the line $x_2 = 0.4$, illustrating that both values are consistent. Therefore, we conclude that the proposed topological derivative is accurate.

4.3. Band calculation

In the previous experiments, we have focused on a single resonant wavenumber. However, we are often interested in how the eigenvalue depends on the

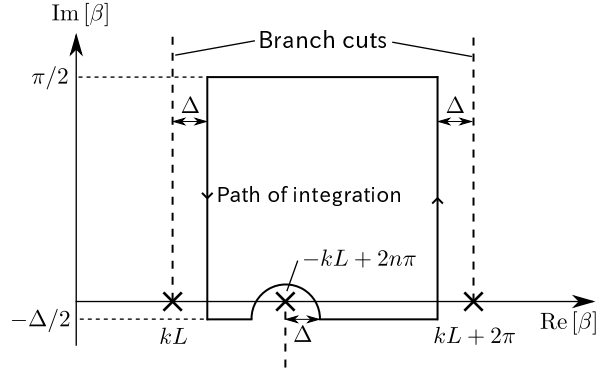


Figure 11: Path of integration used in the SSM algorithm for band calculation. The crosses denote the branch points of the function $\beta \mapsto T^G(\omega, \beta)$, and the dashed lines denote the corresponding cuts.

frequency, i.e., phononic band structure. Because of the quasiperiodicity and time-reversal symmetry, it suffices to find eigenvalues in $\{\beta \in \mathbb{C} \mid kL < \text{Re}[\beta] < kL + 2\pi, \text{Im}[\beta] \geq 0\}$ for a fixed ω . In the following numerical experiment, we set a path of integration C for the SSM algorithm (Figure 11) with $\Delta = 0.01$.

Figure 12 (a) shows the plot of the band structure obtained using the proposed method. In the diagram, the computed eigenvalues β are replaced with $\beta + 2m\pi$, where m is an integer that satisfies $0 \leq \text{Re}[\beta + 2m\pi] \leq \pi$. The obtained band diagram has some similar features to that of planar waveguides [19]. For example, the diagram (Figure 12 (a)) shows that the third band departs from the lightline at around $\omega = 6.2$ (cutoff frequency). In addition, the first band $\omega(\beta)$ satisfies $\hat{c}\beta/L \leq \omega(\beta) \leq c\beta/L$. They are typical characteristics of the waveguide dispersion. The figure shows that the eigenvalues outside the radiation continuum, which is the region below the lightlines, have small imaginary parts, thus forming guided modes along the periodic structure. Within the radiation continuum (gray-shaded region in Figure 12 (a)), almost every eigenmode is leaky due to its nonzero imaginary part. However, we find a significantly small imaginary part within the continuum around $\omega = 3.26$ and 5.16 . Figure 12 (b) shows that the absolute values of the imaginary part decrease rapidly around $\omega = 3.2626$ and $\omega = 5.1577$, indicating that two BICs exist around the points.

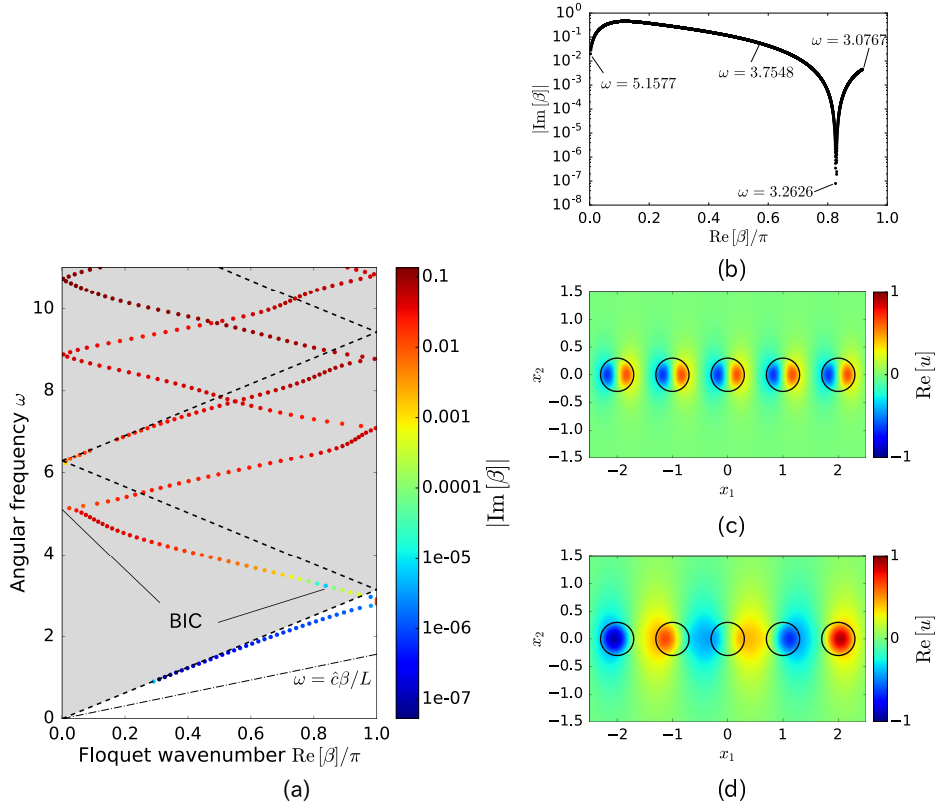


Figure 12: Result of the band calculation and BIC obtained from the analysis. (a) Band structure obtained using SSM. The dashed lines indicate the lightlines $\beta = \pm kL + 2n\pi$ with $n \in \mathbb{Z}$. (b) Imaginary part of the eigenvalues β in $3.0767 \leq \omega \leq 5.1577$. (c) Mode profile of the BIC at $(\omega, \beta) = (5.1580 - 1.1732 \times 10^{-5}i, 0)$. (d) Mode profile of the BIC at $(\omega, \beta) = (3.2626, 2.5952 - 7.9502 \times 10^{-8}i)$.

The latter point stands for a symmetry-protected BIC [1] because it lies on the Γ point ($\beta = 0$). As long as the parity symmetry with respect to $x_1 \rightarrow -x_1$ is preserved and the material parameters satisfy a certain condition, there exists at least one symmetry-protected BIC with $\text{Re}[\beta] = 0$ [40, 41]. Further, we conducted an eigenvalue analysis to find a resonant ω for fixed $\beta = 0$. We obtained that $(\omega, \beta) = (5.1580 - 1.1732 \times 10^{-5}i, 0)$ is an eigenpair, whose mode profile is illustrated in Figure 12 (c). Figure 12 (d) shows the resonant mode corresponding to $(\omega, \beta) = (3.2626, 2.5952 - 7.9502 \times 10^{-8}i)$. From the mode

profiles, we observe that the fields are strongly confined around the structure without radiation. This type of BICs on the second band with $\text{Re}[\beta] \neq 0$ are already reported and discussed for circular inclusions [9, 42].

4.4. Topology optimization

From the previous subsection, we observed that the periodic array of circular cylinders exhibits some BICs. Although only the two BICs are found in the band diagram, the existence of BICs in a higher frequency regime is reported for a simple geometry [40]. In this section, we show that the topology optimization can realize a new BIC for a given higher frequency.

We use the same material parameters as previous experiments. Using the topology optimization, we minimize the imaginary part of the resonant wavenumber $\beta = 2.10 + 0.586i$ at $\omega = 10.0$ of the periodic structure shown in Figure 8. To this end, we set the objective functional J as $J = (\text{Im}[\beta])^2$ and determine an optimized unit structure within the fixed design domain $[-0.354, 0.354] \times [-0.354, 0.354]$, so that it exhibits a BIC if J attains the value of zero. The size of the fixed design domain is chosen to avoid violating the well-separated condition (described in Section 2.3).

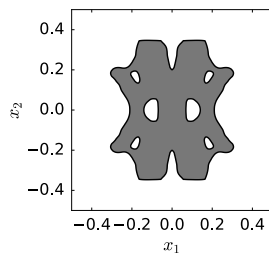


Figure 13: Optimized shape of a unit structure.

Figure 13 and 14 show the results of the topology optimization. We obtain the optimized shape shown in Figure 13 using the topology optimization for the unit structure. This structure has a resonant wavenumber of $\beta = 1.00 + 0.109 \times 10^{-14}i$ (corresponding to the objective value $J = 1.19 \times 10^{-30}$) at $\omega = 10.0$. Figure 14 (b) shows the convergence history of J . The figure shows

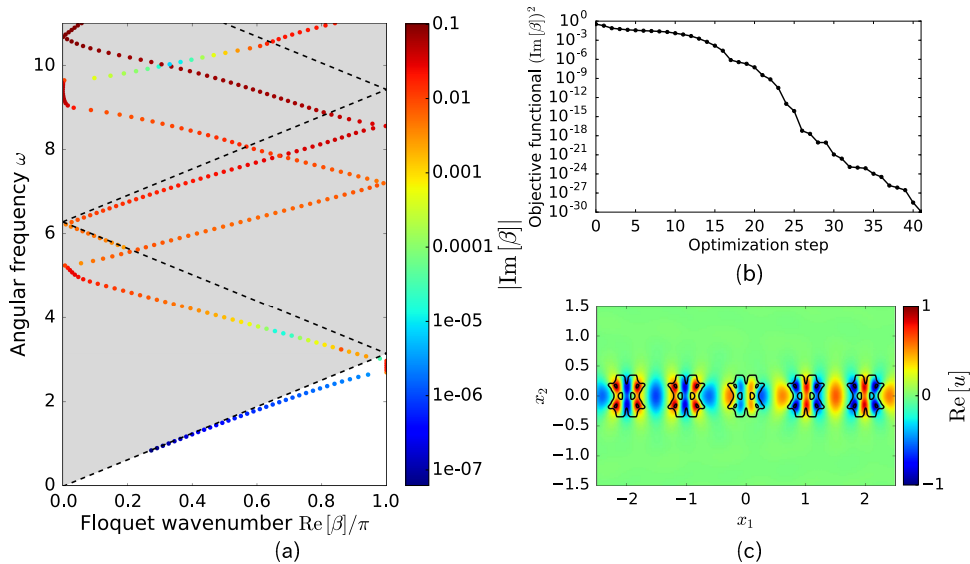


Figure 14: Result of the topology optimization. (a) Band structure for the optimized structure. (b) Convergence history of the optimization. (c) Mode profile of the BIC at $(\omega, \beta) = (10.0, 1.00 + 0.109 \times 10^{-14}i)$.

that the topology optimization successfully decreases the value of J . We also conduct a band analysis for the optimized shape and plot the band structure in Figure 14 (a). From the band structure, we observe that the optimized shape has small imaginary parts around $\omega = 10.0$, whereas the initial shape has relatively large imaginary parts (Figure 12 (a)). Although the obtained eigenvalue has a significantly small imaginary part, we cannot guarantee that this is a true BIC because of numerical errors that arise in the BEM and SSM.

To show that the optimized structure supports a guided wave at the desired frequency $\omega = 10.0$, we investigate the scattering of the cylindrical wave $H_0^{(1)}(k|\mathbf{x} - \mathbf{x}_{\text{source}}|)$ through the optimized array with source point $\mathbf{x}_{\text{source}} = (-1.0, 0.0)^T$ (Figure 15). We compute the energy fluxes E_{in} and E_{out} across the lines $\Gamma_{\text{in}} = \{\mathbf{x} \in \mathbb{R}^2 \mid x_1 = 0.5, -0.5 < x_2 < 0.5\}$ and $\Gamma_{\text{out}} = \{\mathbf{x} \in \mathbb{R}^2 \mid x_1 = 19.5, -0.5 < x_2 < 0.5\}$, respectively. Figure 15 (b) shows the plot of the transmittance $E_{\text{out}}/E_{\text{in}}$ and frequency. The figure shows that the spectrum has peaks at $\omega = 3.6$ and 10.0 , corresponding to the eigenvalues with small imagi-

nary parts in Figure 14 (a). Figure 15 (c) and (d) show the total field u when the incident wave illuminates the array for $\omega = 8.0$ and $\omega = 10.0$, respectively. We also plot the real part of the total field at $\omega = 10.0$ in Figure 15 (e); it shows the similar wave profile to the new BIC (Figure 14 (c)). These results show that the incident field excites the guided mode (BIC) at $\omega = 10.0$ realized by the topology optimization; however, it exhibits no coupling to any guided mode for $\omega = 8.0$.

We can also observe a BIC by finding Wood's anomaly in a scattering analysis [43]. As shown in Figure 16 (a), we analyze the scattering of a plane wave by the optimized structure. The incident angle θ^{in} is given by $\theta^{\text{in}} = 5.74$ deg so that the line $\beta = kL \sin \theta^{\text{in}}$ crosses the band at $\omega = 10.0$ as shown in Figure 16 (b). Figure 16 (c) shows the reflectance, which is defined by the downward energy flux divided by the incident energy flux per unit cell, versus the angular frequency. The spectrum exhibits a sharp resonance at $\omega = 10.0$, corresponding to the BIC realized through the topology optimization. Further analyses show that a solution of the scattering problem is not unique at exact BICs [40, 41].

In the band diagram shown in Figure 14 (a), the optimized BIC occurs at the crossing of two bands. To check whether this is a necessary condition for realizing a BIC, we conduct the same topology optimization at the frequency $\omega = 9.48$ with resonant wavenumber $\beta = 1.15 + 0.293i$ in the initial diagram, shown in Figure 12 (a). The optimized geometry and diagram are plotted in Figure 17. The results show that the obtained BIC with $\beta = 0.615 + 4.22 \times 10^{-5}i$ is not a crossing point in the diagram, meaning that the crossing is not a necessary condition.

5. Conclusions

This study proposed a topology optimization scheme for designing resonant waveguides exhibiting BICs at desired frequencies in the two-dimensional space. We formulated the periodic problem using the scattering matrix of a unit structure and computed resonant wavenumbers using the BEM and SSM. Moreover,

we derived a topological derivative of resonant wavenumbers. In the numerical experiments, we first demonstrated that the proposed method determines a resonant wavenumber accurately. Subsequently, we performed a topology optimization to realize a new BIC at a given frequency. Although we considered Helmholtz' equation for a singly periodic system in two dimensions, the underlying idea, which is the combination of BEM, SSM, and topology optimization, would be applicable to two-dimensional problems and other wave fields governed by Maxwell's equations or elastodynamics.

Acknowledgements

The authors would like to acknowledge anonymous referees for their valuable comments. This work was supported by JSPS KAKENHI Grant Numbers JP19J21766 and JP19H00740.

References

- [1] C. W. Hsu, B. Zhen, A. D. Stone, J. D. Joannopoulos, M. Soljačić, Bound states in the continuum, *Nature Reviews Materials* 1 (9) (2016) 1–13. doi:10.1038/natrevmats.2016.48.
- [2] J. von Neumann, E. P. Wigner, über merkwürdige diskrete Eigenwerte, *Physikalische Zeitschrift* 30 (1929) 465–467.
- [3] Y. Plotnik, O. Peleg, F. Dreisow, M. Heinrich, S. Nolte, A. Szameit, M. Segev, Experimental observation of optical bound states in the continuum, *Physical Review Letters* 107 (18) (2011) 183901. doi:10.1103/PhysRevLett.107.183901.
- [4] J. Lee, B. Zhen, S.-L. Chua, W. Qiu, J. D. Joannopoulos, M. Soljačić, O. Shapira, Observation and differentiation of unique high- Q optical resonances near zero wave vector in macroscopic photonic crystal slabs, *Physical Review Letters* 109 (6) (2012) 067401. doi:10.1103/PhysRevLett.109.067401.

- [5] C. W. Hsu, B. Zhen, J. Lee, S.-L. Chua, S. G. Johnson, J. D. Joannopoulos, M. Soljačić, Observation of trapped light within the radiation continuum, *Nature* 499 (7457) (2013) 188–191. doi:10.1038/nature12289.
- [6] C. M. Linton, P. McIver, Embedded trapped modes in water waves and acoustics, *Wave Motion* 45 (1) (2007) 16–29. doi:10.1016/j.wavemoti.2007.04.009.
- [7] F. Dreisow, A. Szameit, M. Heinrich, R. Keil, S. Nolte, A. Tünnermann, S. Longhi, Adiabatic transfer of light via a continuum in optical waveguides, *Optics Letters* 34 (16) (2009) 2405–2407. doi:10.1364/OL.34.002405.
- [8] Y. Yang, C. Peng, Y. Liang, Z. Li, S. Noda, Analytical perspective for bound states in the continuum in photonic crystal slabs, *Physical Review Letters* 113 (3) (2014) 037401. doi:10.1103/PhysRevLett.113.037401.
- [9] E. N. Bulgakov, A. F. Sadreev, Bloch bound states in the radiation continuum in a periodic array of dielectric rods, *Physical Review A* 90 (5) (2014) 053801. doi:10.1103/PhysRevA.90.053801.
- [10] A. Kodigala, T. Lepetit, Q. Gu, B. Bahari, Y. Fainman, B. Kanté, Lasing action from photonic bound states in continuum, *Nature* 541 (7636) (2017) 196–199. doi:10.1038/nature20799.
- [11] J. M. Foley, S. M. Young, J. D. Phillips, Symmetry-protected mode coupling near normal incidence for narrow-band transmission filtering in a dielectric grating, *Physical Review B* 89 (16) (2014) 165111. doi:10.1103/PhysRevB.89.165111.
- [12] A. A. Yanik, A. E. Cetin, M. Huang, A. Artar, S. H. Mousavi, A. Khanikaev, J. H. Connor, G. Shvets, Hatice Altug, Seeing protein monolayers with naked eye through plasmonic Fano resonances, *Proceedings of the National Academy of Sciences* 108 (29) (2011) 11784–11789. doi:10.1073/pnas.1101910108.

- [13] J. Sokolowski, J.-P. Zolesio, Introduction to Shape Optimization: Shape Sensitivity Analysis, Springer Series in Computational Mathematics, Springer, Berlin, Heidelberg, 1992.
- [14] M. P. Bendsøe, O. Sigmund, Topology Optimization: Theory, Methods, and Applications, Springer Science & Business Media, 2013.
- [15] D. C. Dobson, S. J. Cox, Maximizing band gaps in two-dimensional photonic crystals, *SIAM Journal on Applied Mathematics* 59 (6) (1999) 2108–2120. doi:10.1137/S0036139998338455.
- [16] D. Evans, R. Porter, Trapped modes embedded in the continuous spectrum, *Quarterly Journal of Mechanics and Applied Mathematics* 51 (2) (1998) 263–274. doi:10.1093/qjmam/51.2.263.
- [17] R. Porter, D. V. Evans, Embedded Rayleigh–Bloch surface waves along periodic rectangular arrays, *Wave Motion* 43 (1) (2005) 29–50. doi:10.1016/j.wavemoti.2005.05.005.
- [18] L. G. Bennetts, M. A. Peter, Rayleigh–Bloch waves above the cutoff, *Journal of Fluid Mechanics* 940. doi:10.1017/jfm.2022.247.
- [19] J. Hu, C. R. Menyuk, Understanding leaky modes: Slab waveguide revisited, *Advances in Optics and Photonics* 1 (1) (2009) 58–106. doi:10.1364/AOP.1.000058.
- [20] H. Ammari, A. Dabrowski, B. Fitzpatrick, P. Millien, Perturbation of the scattering resonances of an open cavity by small particles. Part I: The transverse magnetic polarization case, *Zeitschrift für angewandte Mathematik und Physik* 71 (4) (2020) 102. doi:10.1007/s00033-020-01324-6.
- [21] Z. Gimbutas, L. Greengard, Fast multi-particle scattering: A hybrid solver for the Maxwell equations in microstructured materials, *Journal of Computational Physics* 232 (1) (2013) 22–32. doi:10.1016/j.jcp.2012.01.041.

- [22] J. Sokolowski, A. Zochowski, On the topological derivative in shape optimization, *SIAM Journal on Control and Optimization* 37 (4) (1999) 1251–1272. doi:10.1137/S0363012997323230.
- [23] H. Isakari, T. Takahashi, T. Matsumoto, A topology optimisation with level-sets of B-spline surface (in Japanese), *Transactions of the Japan Society for Computational Methods in Engineering* 17 (2017) 125–130.
- [24] A. J. Burton, G. F. Miller, J. H. Wilkinson, The application of integral equation methods to the numerical solution of some exterior boundary-value problems, *Proceedings of the Royal Society of London. A. Mathematical and Physical Sciences* 323 (1553) (1971) 201–210. doi:10.1098/rspa.1971.0097.
- [25] C.-J. Zheng, H.-B. Chen, H.-F. Gao, L. Du, Is the Burton–Miller formulation really free of fictitious eigenfrequencies?, *Engineering Analysis with Boundary Elements* 59 (2015) 43–51. doi:10.1016/j.enganabound.2015.04.014.
- [26] M. Abramowitz, I. A. Stegun, *Handbook of Mathematical Functions with Formulas, Graphs, and Mathematical Tables*, Dover Publications, 1965.
- [27] P. A. Martin, *Multiple Scattering: Interaction of Time-harmonic Waves with N Obstacles*, Cambridge University Press, 2006.
- [28] R. Coifman, V. Rokhlin, S. Wandzura, The fast multipole method for the wave equation: A pedestrian prescription, *IEEE Antennas and Propagation Magazine* 35 (3) (1993) 7–12. doi:10.1109/74.250128.
- [29] N. A. Nicorovici, R. C. McPhedran, L. C. Botten, Photonic band gaps for arrays of perfectly conducting cylinders, *Physical Review E* 52 (1) (1995) 1135–1145. doi:10.1103/PhysRevE.52.1135.
- [30] C. M. Linton, Schlömilch series that arise in diffraction theory and their efficient computation, *Journal of Physics A: Mathematical and General* 39 (13) (2006) 3325–3339. doi:10.1088/0305-4470/39/13/012.

- [31] R. Porter, D. V. Evans, Rayleigh–Bloch surface waves along periodic gratings and their connection with trapped modes in waveguides, *Journal of Fluid Mechanics* 386 (1999) 233–258. doi:10.1017/S0022112099004425.
- [32] Y. Otani, N. Nishimura, An FMM for periodic boundary value problems for cracks for Helmholtz’ equation in 2D, *International Journal for Numerical Methods in Engineering* 73 (3) (2008) 381–406. doi:10.1002/nme.2077.
- [33] H. Isakari, K. Niino, H. Yoshikawa, N. Nishimura, Calderon’s preconditioning for periodic fast multipole method for elastodynamics in 3D, *International Journal for Numerical Methods in Engineering* 90 (4) (2012) 484–505. doi:10.1002/nme.3332.
- [34] T. Nose, N. Nishimura, Calculation of eigenvalues related to 2 dimensional periodic boundary value problems for the Helmholtz equation using the Sakurai-Sugiura method and periodic fast multipole method (in Japanese), *Transactions of the Japan Society for Industrial and Applied Mathematics* 24 (2014) 185–201.
- [35] R. Misawa, K. Niino, N. Nishimura, An FMM for waveguide problems of 2-D Helmholtz’ equation and its application to eigenvalue problems, *Wave Motion* 63 (2016) 1–17. doi:10.1016/j.wavemoti.2015.12.006.
- [36] T. Ooura, M. Mori, A robust double exponential formula for Fourier-type integrals, *Journal of Computational and Applied Mathematics* 112 (1) (1999) 229–241. doi:10.1016/S0377-0427(99)00223-X.
- [37] J. Asakura, T. Sakurai, H. Tadano, T. Ikegami, K. Kimura, A numerical method for nonlinear eigenvalue problems using contour integrals, *JSIAM Letters* 1 (2009) 52–55. doi:10.14495/jsiaml.1.52.
- [38] K. Nakamoto, H. Isakari, T. Takahashi, T. Matsumoto, A level-set-based topology optimisation of carpet cloaking devices with the boundary element method, *Mechanical Engineering Journal* 4 (1) (2017) 16–00268. doi:10.1299/mej.16-00268.

- [39] S. Amstutz, H. Andrä, A new algorithm for topology optimization using a level-set method, *Journal of Computational Physics* 216 (2) (2006) 573–588. doi:10.1016/j.jcp.2005.12.015.
- [40] A.-S. Bonnet-Bendhia, F. Starling, Guided waves by electromagnetic gratings and non-uniqueness examples for the diffraction problem, *Mathematical Methods in the Applied Sciences* 17 (5) (1994) 305–338. doi:10.1002/mma.1670170502.
- [41] S. P. Shipman, Resonant scattering by open periodic waveguides, in: *Progress in Computational Physics*, Vol. 1, Bentham Science Publishers, 2010.
- [42] L. Yuan, Y. Y. Lu, Bound states in the continuum on periodic structures surrounded by strong resonances, *Physical Review A* 97 (4) (2018) 043828. doi:10.1103/PhysRevA.97.043828.
- [43] F. Monticone, A. Alù, Bound states within the radiation continuum in diffraction gratings and the role of leaky modes, *New Journal of Physics* 19 (9) (2017) 093011. doi:10.1088/1367-2630/aa849f.

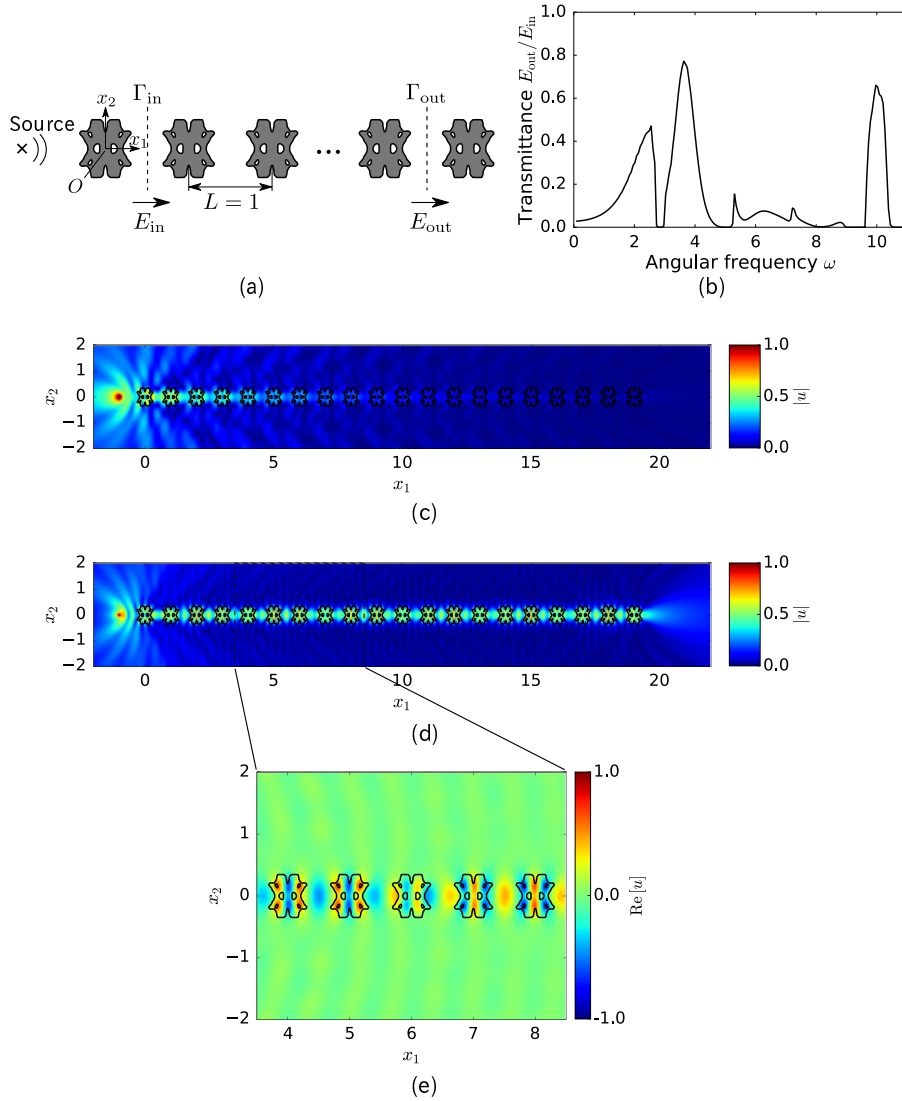


Figure 15: Scattering of a cylindrical wave by the optimized structure. (a) Array of the optimized unit structure; the array comprises 20 scatterers. (b) Transmittance spectrum of guided waves along the structure. (c) Intensity of the total field for $\omega = 8.0$. (d) Intensity of the total field for $\omega = 10.0$. (e) Real part of the total field for $\omega = 10.0$.

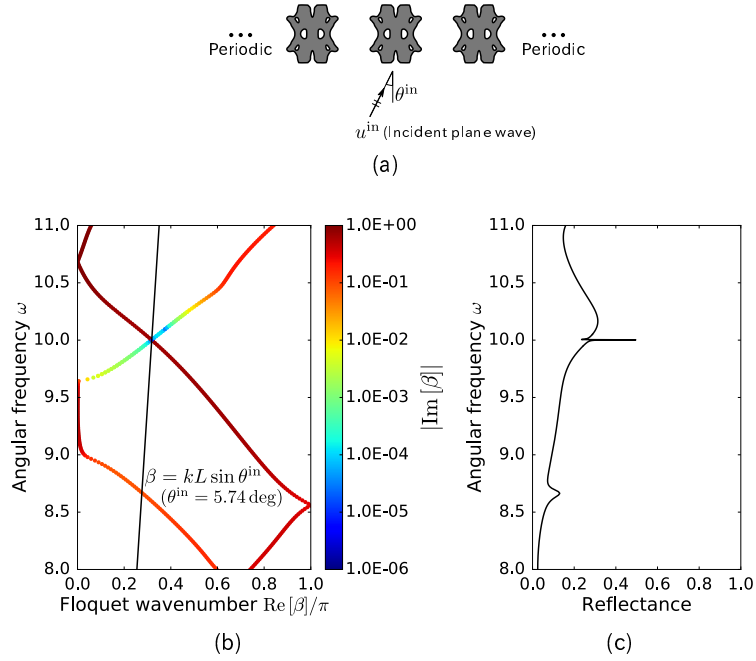


Figure 16: Scattering of a plane wave by the optimized periodic structure. (a) Optimized periodic structure. (b) Band structure. (c) Reflectance spectrum for $\theta^{\text{in}} = 5.74$ deg.

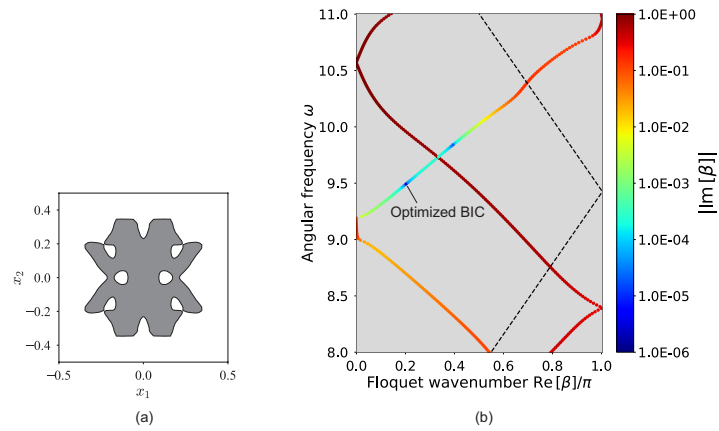


Figure 17: Optimized structure (a) and band diagram (b) for the target resonant pair $(\omega, \beta) = (9.48, 1.15 + 0.293i)$.